Sci

MDPI

Article

Study of Structure and Properties of Thin-Walled Elements of Diamond Cellular Structures Made of Aluminum Alloys via Selective Laser Melting

Tatiana Tarasova *, Pavel Podrabinnik, Nikolay Babushkin, Andrey Gusarov, Roman Khmyrov, Daniil Strunevich and Sergey N. Grigoriev

Department of High Efficiency Processing Technologies, Moscow State University of Technology "STANKIN", Vadkovsky Per. 3a, 127055 Moscow, Russia
* Correspondence: t.tarasova@stankin.ru

Abstract: The work is dedicated to the investigation of the possibility of producing and studying the properties of the thin-walled elements of Diamond-type lattice structures, manufactured from the aluminum alloy AlSi10Mg using the selective laser melting method. The accuracy of fabricating the thin-walled elements was assessed depending on the specified model thickness, power, and scanning strategy. It was demonstrated that the minimum wall thickness with minimal porosity was achieved at a laser power of 260 W and a laser scanning speed of 1500 mm/s. Based on the selected SLM parameters, Diamond-type lattice structures with a wall thickness of 200 μm were produced. Tomographic methods confirmed minimal deviation in the thickness and shape of the lattice structure from the model. Mechanical compression tests were conducted to determine the deformation characteristics, as well as the Young's modulus, yield strength, and ultimate tensile strength. It was shown that the chosen parameters allow for the production of functional lattice structures.

Keywords: additive technologies; selective laser melting; aluminum alloys; lattice structures; cellular structures; thin walls

Citation: Tarasova, T.; Podrabinnik, P.; Babushkin, N.; Gusarov, A.; Khmyrov, R.; Strunevich, D.; Grigoriev, S.N. Study of Structure and Properties of Thin-Walled Elements of Diamond Cellular Structures Made of Aluminum Alloys via Selective Laser Melting. *Sci* **2024**, *6*, 85. https://doi.org/10.3390/sci6040085

Received: 24 September 2024
Revised: 8 November 2024
Accepted: 12 December 2024
Published: 20 December 2024

1. Introduction

Additive technologies (ATs), which have been rapidly developing in recent years, provide the opportunity to manufacture complex-shaped parts directly from computer models, bypassing labor-intensive operations for creating special molds, tooling, and equipment setups. Their wide demand is driven by their flexibility and ability to produce finished products from digital models quickly. This has radically changed the technology of product development in machine engineering [1]. Methodologies for filling the volume of a part with a system of rods and shells instead of solid material have been developed, which can significantly reduce weight while maintaining mechanical characteristics at acceptable levels. Lattice structures, also known as cellular structures, have applications in various industrial sectors due to their unique characteristics such as low elastic modulus, high stiffness-to-weight ratio, low thermal expansion coefficient, and large specific surface area. Lattice structures manufactured using traditional production technologies always involve complex process control, additional assembly stages, or other uncontrollable factors. Additive manufacturing technologies, based on layer-by-layer fabrication using computer-aided design models, enable the production of complex components like lattice structures, leading to effective processing time reduction and minimal material waste. Thus, additive manufacturing removes structural design limitations and ensures the precise fabrication of lattice structures with good quality. Active research is being conducted on developing additive manufacturing technologies for metallic lattice structures [2,3].

Today, scientific studies on the fabrication of metallic lattice constructions using selective laser melting (SLM) are underway to obtain products with good mechanical

properties and low weight, which are in demand in the aerospace, energy, and chemical industries. The SLM process involves the layer-by-layer fabrication of a part from powder by locally melting the powder with a focused laser beam that scans each layer according to its electronic model [1,4]. This layer-by-layer formation method for powder materials has already been adopted by the industry for most traditionally used metals and alloys [4–7].

The fundamental principles of designing metallic lattice structures for manufacturing via AT methods have been developed. However, their production and implementation are limited due to the lack of refined manufacturing technologies. Applying SLM to the fabrication of metallic lattice structures faces fundamental challenges because the size of volumetric (pores and microcracks) and surface (relief) defects, as well as dimensional deviations, is comparable to the thickness of the elements of lattice structures.

The SLM process is significantly influenced by a large number of process parameters, such as laser power, laser spot diameter, scanning speed and strategy, and powder layer thickness, as well as the parameters of the feedstock material. Therefore, one of the key problems of SLM technology is the optimization of process parameters to achieve stable process modes and reduce the number of mentioned defects [6]. Often, this involves a compromise between material quality and process productivity [7]. Additive technologies in general, and SLM in particular, allow for significant complexity in the geometric shape of parts, opening up broad opportunities for topological optimization. Various periodic lattice structures made from metal alloys have been produced using SLM, demonstrating good mechanical properties [8,9]. These structures can consist of either rods or shells. Numerous types of morphologies for such structures have been proposed to optimize their various properties [10].

To build periodic rod structures, an analogy with crystal lattices is often used (e.g., simple cubic, Diamond, and fluorite structures), where rods are drawn along the shortest distances between nodes. Another method is based on densely filling spaces with polyhedra, such as truncated octahedra (the so-called Kelvin foam) or rhombicosidodecahedra, where rods traverse the edges of these polyhedra. Among structures built from shells, various triply periodic minimal surfaces, particularly gyroids, are in demand. Besides morphology, the ratio of rod diameter or shell thickness to the structure's period can be defined, allowing for changes in weight, porosity, specific surface area, and other characteristics. The ratio of the structure size to the unit cell is an important parameter for achieving convergence and minimizing boundary effects. The ratio proposed by the authors is seven times greater than the rod diameter in all three directions. The mentioned structures are often considered not as standalone products but as elements filling the volume of a part instead of solid material, whose advantages include weight reduction, reduced material consumption, and lower thermal conductivity [11–13]. Such materials do not necessarily have a periodic structure; the structure can be stochastic or gradient. For prosthetic applications, stochastic rod structures resembling bone tissue have been produced from pure titanium using SLM. Digital models for these structures were generated using the pseudo-randomization of the periodic structure. Gradient micro-lattices were created by spatially modulating the thickness of rods [14,15].

A significant number of models for lattice structures and methodologies for their construction have been developed to date [16,17]. Nevertheless, theoretical research in this area continues. In order to determine the optimal design of lattice structures, it is essential to establish a clear relationship between the structural parameters and the characteristics of the beam nodes in the lattice design. Moreover, the adaptation of models to specific manufacturing technologies is of particular interest. Many studies have focused on the fabrication of metallic lattice structures using various additive manufacturing methods and the experimental investigation of their structure and properties. Below are examples where metallic structures were obtained through selective laser melting (SLM) technology.

Al-Ketan et al. [8] conducted static compression tests on beam and shell lattice structures with various morphologies made from martensitic aging steel. According to all measured mechanical characteristics, namely stiffness, strength, and fracture toughness, significant advantages were observed for shell structures based on triply periodic minimal surfaces. In another study [18], periodic beam structures were fabricated from the aluminum alloy AlSi10Mg, and their specimens were subjected to compression tests, revealing various failure mechanisms and measuring the compressive strength limit as a function of structure morphology and lattice period. Maskeri et al. [19] produced shell structures in the shape of gyroids from the same alloy and tested them under static compression. Additionally, Zha et al. [20] investigated the mechanical properties of shell structures made from triply periodic minimal surfaces using austenitic steel AISI 316 L. Beyond mechanical properties, the thermal conductivity of cellular metallic materials produced by SLM is also being studied [21].

Much attention is paid to the study of Diamond-type cellular structures, which are triply periodic minimal surface (TPMS) structures, due to their demand in applications requiring compression and energy absorption. Khanna et al. showed that AlSi10Mg Diamond structures outperformed gyroid, Schwartz, and Lidinoid structures in strength and the modulus of compression and energy absorption [22]. It is also noted that the type of lattice deformation depends on the relative density of the structure. Yan et al. showed that there is a direct dependence between the compressive modulus and strength of structures and their volume fraction and unit size in Diamond lattice structures made of AlSi10Mg. However, the strut size of the Diamond lattice must be strictly controlled as it is normally greater than designed, affecting relative density [23]. Soul et al. reported that the mechanical properties of Diamond structures depend greatly on the orientation of Diamond cells [24]. Yu et al. studied the deformation mechanism of the AlSi10Mg Diamond structure, which was found to be bend-dominated [25]. In turn, Nie et al. tested four different types of Diamond lattice structures, namely uniform skeletal (USK), uniform sheet (USH), grade skeletal (GSK), and grade sheet, and found that graded structures exhibited layer-by-layer failure, while sheet structures showed brittle fracture [26]. Song et al. established that sheet structures had more stable deformation patterns than the skeletal ones, which contributed to energy absorption capacity [27]. The performance of Diamond lattice structures depends not only on accuracy and relative density but also on the oxygen content in building chambers. Baroutaji et al. showed an increase in ductility by ~5.7% and 2% in toughness, plateau stress, and specific energy absorption [28].

The presence of manufacturing defects and deviations from the model was qualitatively assessed using electron microscopy images [29,30], quantitatively measured through the density of the samples [21], and analyzed via three-dimensional X-ray tomographic imaging [14,20]. Choy et al. investigated the mechanical properties of uniform and gradient lattices made from the titanium alloy Ti6Al4V based on their orientation [31].

Thus, the main research directions are the following:

- The development of design principles for metallic lattice structures adapted to specific additive manufacturing technologies, which optimize the desired properties.
- The fabrication of metallic lattice structures using additive manufacturing methods and the study of their structure and properties.

It should be noted that the influence of the microstructure defects of thin elements in metallic lattice structures manufactured by the SLM method, as well as dimensional deviations from the model, on the properties of the resulting constructions requires further investigation. This is essential for optimizing SLM parameters when fabricating metallic lattice structures with the required product characteristics.

In the present work, studies were conducted on the accuracy of the shape production of thin-walled elements and shell lattice structures made from the aluminum alloy AlSi10Mg using the SLM method, alongside the influence of processing parameters on their microstructure and properties.

2. Materials and Methods

2.1. Raw Materials and Additive Manufacturing

The material chosen for sample fabrication was a fine-dispersed powder of the aluminum alloy AlSi10Mg (UC "Rusal", Moscow, Russia) with a declared particle size distribution of 20–63 microns (Figure 1). Aluminum alloys are actively used for manufacturing structural components in aerospace engineering, and the reduction in part weight obtained through the use of cellular structures is particularly relevant.

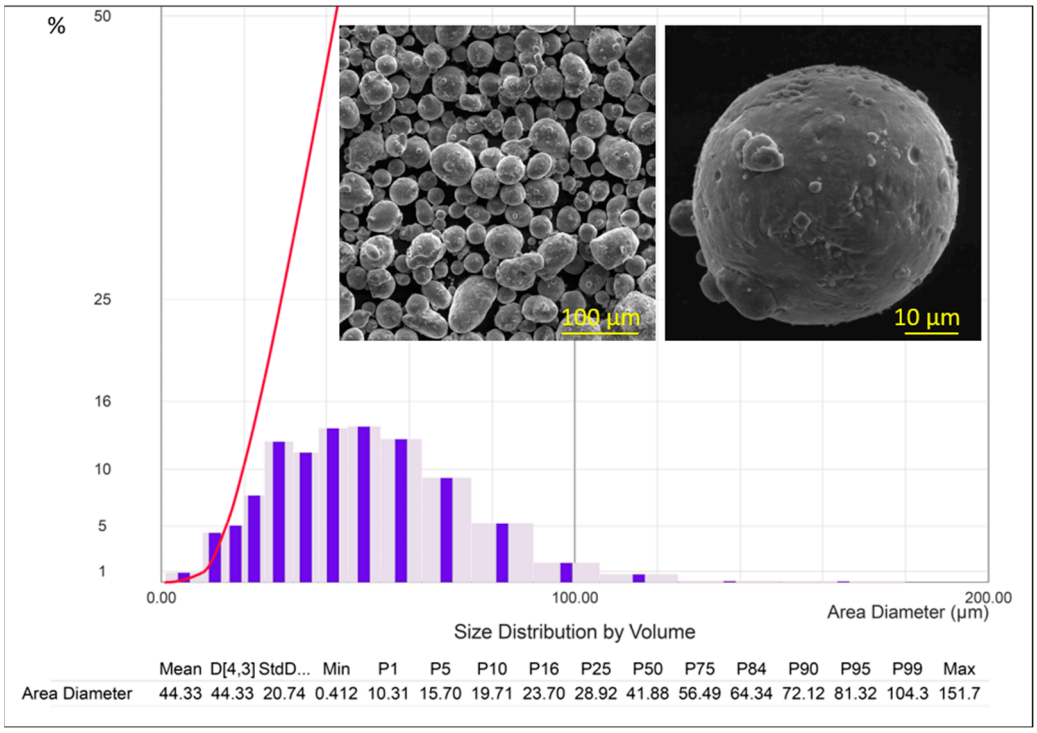

Figure 1. Granulometry of AlSi10Mg powder.

To confirm the particle size and elemental composition, the powder was also analyzed using a Tescan Vega 3 LMH scanning electron microscope (Tescan, Brno, Czech Republic) equipped with an energy-dispersive analysis (EDX) X-Act module (Oxford Instruments, Abington, UK). The circularity factor of the powder was found to be 0.682, which is sufficient for the stable application of a uniform and homogeneous layer. The spherical shape of the particles allows for more compact and tight packing within a given volume, ensuring the flowability of the powder composition in material feed systems with minimal resistance. The elemental composition of the powder meets the declared specifications (Table 1).

Table 1. AlSi10Mg powder composition.

Material	Element, % Mass.						
	Al	Si	Mg	Fe	Ni	Cu	Mn
AlSi10Mg	bal.	9.88 ± 0.2	0.33 ± 0.1	0.1	0.2	-	0.1

The samples were manufactured using a Farsoon FS121M industrial selective laser melting (SLM) system (Farsoon Technologies, Changsha, China). The machine was equipped with a 500 W Nd:YAG laser with a wavelength of 1064 nm and a laser beam diameter of 50 µm. During the printing process, the parameters of laser power P, scanning speed V, and the wall thickness of a digital model were varied. To ensure a single-scanning strategy

for the single-scan walls, a solid block was modeled, in which the hatch distance parameter was increased to 2 mm.

2.2. Microstructure Characterization, Linear Measurements, and Mechanical Tests

Testing the accuracy of the produced thin-walled elements, microstructure analysis, and defect assessment were conducted using an OLYMPUS BX 51M optical microscope (Olympus, Tokyo, Japan), as well as scanning electron microscopy (SEM). To evaluate the mechanical properties of the thin-walled elements, designs based on Diamond-type shells were selected. The outer linear dimensions of the samples were measured using a coordinate method with a GLOBAL 050,505 coordinate measuring machine (Hexagon, Stockholm, Sweden). The mass of the samples was determined using GR-300 laboratory electronic scales (A&D, Tokyo, Japan).

Additionally, the obtained Diamond structures were further investigated using computed tomography with a Nordson DAGE system (Nordson, Westlake, OH, USA), capable of recognizing objects with a minimum size of 100 microns, to control the wall thickness of the lattice structures.

The compression tests of the cellular structures were conducted on an Instron 5989 universal electromechanical testing machine (Instron, Norwood, MA, USA) following ASTM E8-08 standards [32]. During the compression tests, the relationship between compressive force F and displacement was established in the compression diagram of the sample. A load was applied to achieve a strain rate of 0.02 mm/s. The direction of the applied load coincided with the direction of the samples' growth.

2.3. Modeling Cell Structures

The modeling of lattice structures based on Diamond-type shells was performed using the widely used CAD system Materialize Magics, which is designed for preparing models for additive manufacturing. This system features a specialized structures module for creating standard lattice structures with various cell sizes.

3. Results and Discussion

The study of the microstructure and properties of the thin-walled elements of lattice structures made from an AlSi10Mg alloy was conducted on samples manufactured using the selective laser melting (SLM) method while varying process parameters such as laser power, scanning speed, and powder layer thickness. The first stage of optimizing SLM process parameters was carried out by producing single beads. In previous research [33], the parameter window for manufacturing thin-walled samples was investigated: laser power P = 170–340 W and scanning speed V = 300–1500 mm/s with a powder layer thickness of 30 μm. Within this parameter window, walls with a specified thickness of 320 μm were produced and analyzed.

As optimality criteria, the accuracy of the geometric parameters (thickness and height) of the developed model, surface roughness, and porosity of the samples were selected. It was established that the most preferable scanning speed for achieving a high-quality wall, considering productivity, is 1500 mm/s.

In the present study, the dependence of the quality of manufactured thin-walled elements on wall thickness was investigated, as well as the influence of SLM parameters on the quality of the produced samples. Additionally, the possibility of achieving a high-quality minimum wall thickness through single-pass laser scanning was explored. Furthermore, Figure 2 illustrates the configuration of the printing platform for the AlSi10Mg objects used in the investigation. A total of six such platforms were printed.

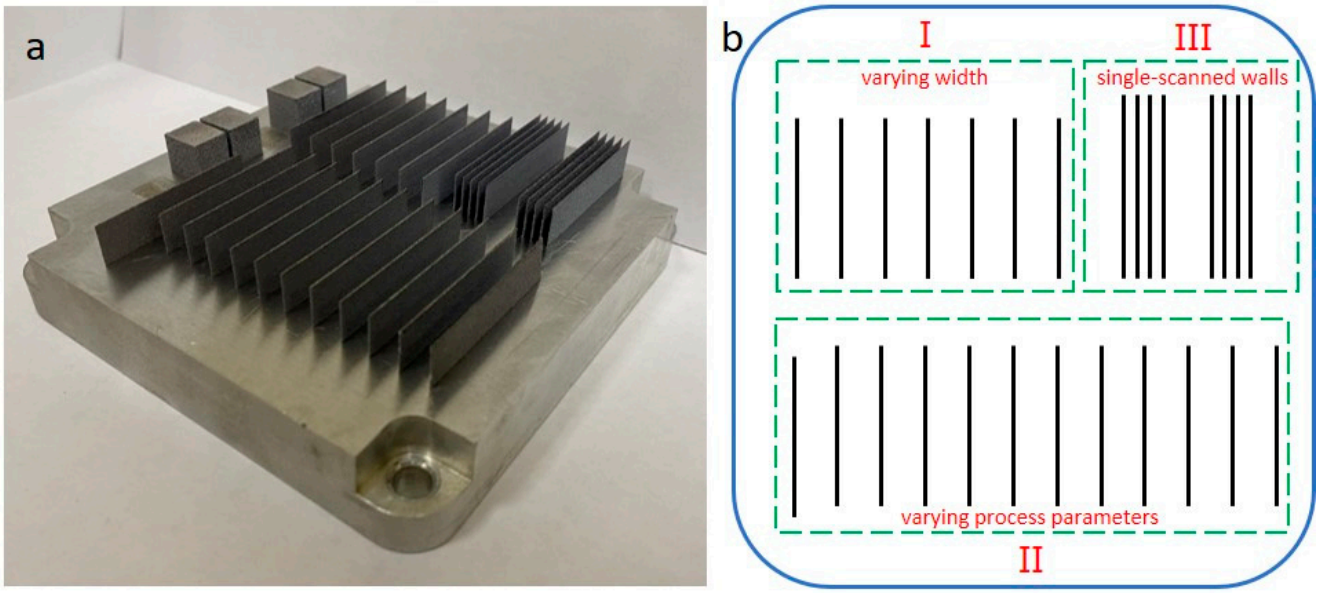

Figure 2. A substrate with the printed samples (**a**); the arrangement of the samples on the substrate (**b**).

3.1. The Influence of Wall Thickness on the Quality of Manufactured Thin-Walled Elements

A series of walls (region I, Figure 2b) was produced according to the nominal model with a variable wall thickness ranging from 150 to 450 µm in increments of 50 µm. These specimens were built with contouring common for the SLM technique. The results of the thickness measurements for the samples are presented in Table 2. The thickness of the samples was evaluated in a cross-section by conducting 10 measurements. From the obtained values, the sample mean was calculated, along with the confidence interval for the deviation of the thickness from the mean at a confidence level of p = 0.95.

Table 2. Change in thickness of thin-walled samples made of AlSi10Mg alloy.

№	Laser Power, W	Scanning Speed, mm/s	Nominal Thickness, µm	Actual Thickness, µm
1	340	1500	150	225.9 ± 13.65
2	340	1500	200	222.8 ± 7.17
3	340	1500	250	279.9 ± 10.57
4	340	1500	300	317.3 ± 6.18
5	340	1500	350	323.9 ± 8.98
6	340	1500	400	434.1 ± 7.34
7	340	1500	450	492.2 ± 15.01

A discrepancy is observed between the specified model thickness and the actual thickness of the samples. Sample No. 2 exhibits the smallest thickness, while Sample No. 1 shows the largest deviation from the model. Additionally, the thickness of the samples increases with the nominal thickness of the model (Figure 3). The appearance of the walls is presented in Figure 4.

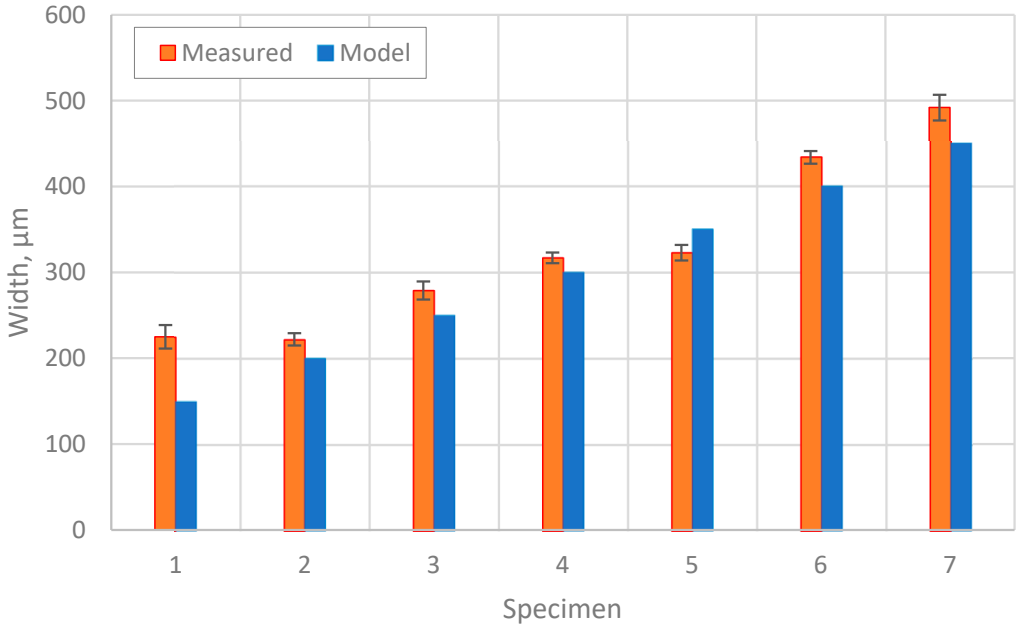

Figure 3. The change in actual wall thickness and its difference from the nominal thickness of the model.

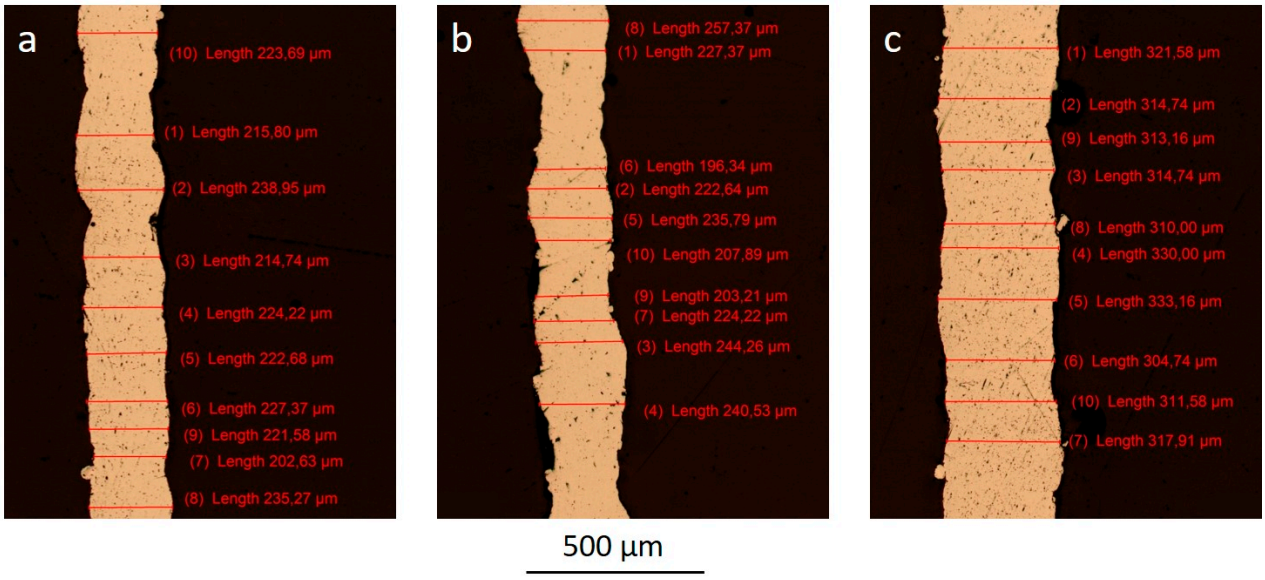

Figure 4. A cross-section of a wall with a nominal thickness of 150 µm (**a**), a cross-section of a wall with a nominal thickness of 200 µm (**b**), and a cross-section of a wall with a nominal thickness of 350 µm (**c**).

3.2. The Influence of Laser Power on Wall Thickness

Table 3 presents the measurement results of the wall thickness of thin-walled samples with varying laser power. The samples (region II, Figure 2b) were printed according to the nominal model of a single wall with a thickness of 270 µm in the printer's slicer. The samples were built up with variable power ranging from 200 W to 470 W while maintaining a constant scanning speed of 1500 mm/s. The contouring was disabled.

Table 3. The influence of the SLM process parameters on the accuracy of the AlSi10Mg thin-walled elements with nominal thickness 270 µm.

№	Thickness, µm	Laser Power, W	Scanning Speed, mm/s
1	161 ± 9.31	200	1500
2	173.2 ± 5.89	230	1500
3	224.4 ± 4.71	260	1500
4	224.2 ± 9.17	290	1500
5	262.8 ± 7.37	320	1500
6	225.9 ± 15.97	350	1500
7	244.3 ± 9.21	380	1500
8	253.8 ± 6.67	410	1500
9	212.2 ± 7.30	440	1500

Figure 5 illustrates a monotonic increase in the thickness of samples from 161 ± 9.31 µm to 262.8 ± 7.37 µm as the laser power increases. This can be attributed to the increasing energy input of the laser radiation, which results in a larger thermal impact zone and an increase in the width of the melt pool.

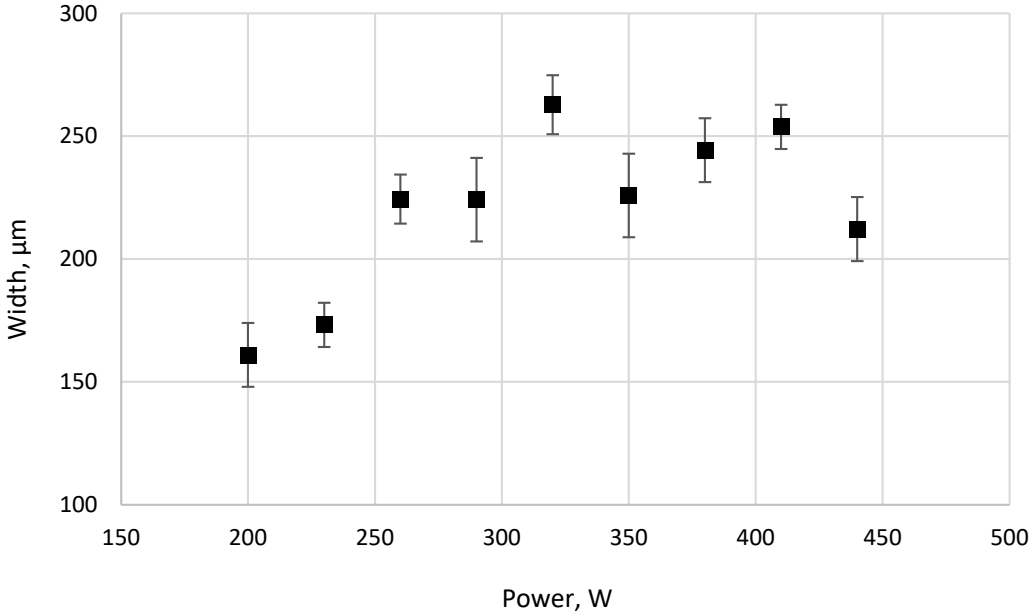

Figure 5. Dependence of wall thickness on laser power.

The minimum wall thickness was achieved at a laser power of P = 200 W; however, this mode did not ensure stable wall formation (Figure 6a). In contrast, increasing the power by 30 W enabled the formation of a stable thin wall with a thickness of 173.2 µm. Meanwhile, wall № 5, produced under the conditions of P = 320 W and V = 1500 mm/s, exhibited a thickness of 262.8 µm, which is the closest to the specified value.

Figure 6 presents cross-sections of the walls, clearly indicating that the thinnest wall is obtained at a laser power of 200 W and a scanning speed of 1500 mm/s (Figure 6a). However, this configuration shows a noticeable lack of fusion evidenced by the periodic interruption of the wall. The most favorable process parameters can be considered as follows: P = 230 W and V = 1500 mm/s.

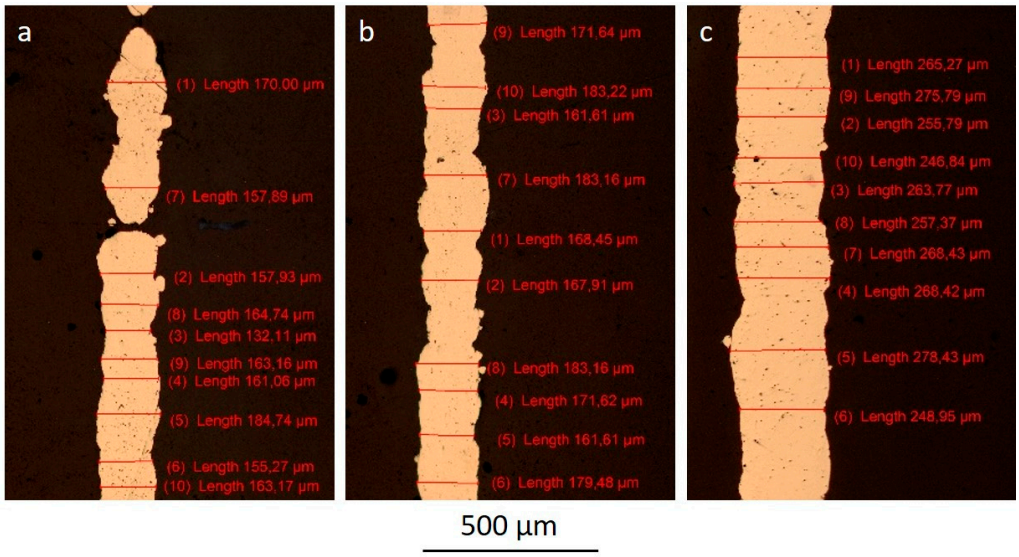

Figure 6. Cross-sections of walls with nominal thickness of 270 µm obtained at laser scanning speed of 1500 mm/s and laser power of 200 W (**a**), 230 W (**b**), and 320 W (**c**).

3.3. The Investigation of the Minimum Possible Wall Thickness in a Single-Scan Strategy

The approaches considered for obtaining thin walls always used a 3D model with a specified thickness as the initial parameter, and the reproduction of which is a task for equipment. In this case, the focus is more on the printing accuracy rather than the machine's capability to achieve the minimum wall thickness. To address this, experiments were conducted to grow thin walls using single-scanning without a predefined 3D model. Solid parallelepipeds were modeled, and a scanning strategy was employed in which the hatch distance was set to 4 mm, enabling scanning in a single direction (region III, Figure 2b). The scanning angle was established along the length of the parallelepiped with a rotation angle of 0 degrees, responsible for adjusting the scanning angle from layer to layer. The scanning speed was set to 1500 mm/s, with the laser power varying from 200 W to 470 W in increments of 30 W. The measurement results of the grown walls are presented in Table 4.

Table 4. The dependence of the parameters of the SLM process on the thickness of the thin-walled samples obtained with a single-scan strategy.

№	Thickness, µm	Porosity, %vol.	Power, W	Scanning Speed, mm/s
1	Discontinuous wall		200	1500
2	144.05 ± 12.97	1.07	230	1500
3	164.55 ± 10.12	0.10	260	1500
4	178.5 ± 12.33	0.75	290	1500
5	198.5 ± 7.91	0.54	320	1500
6	200 ± 9.17	1.38	340	1500
7	183 ± 8.22	0.95	350	1500
8	198 ± 12.65	1.32	380	1500
9	190.5 ± 12.65	1.35	410	1500
10	226.5 ± 11.39	0.68	440	1500
11	224 ± 17.39	2.29	470	1500

With an increase in power, the average wall thickness also increases. This is consistent with the theoretical conclusions made in previous studies that simulated the melt pool geometry as a function of power. As the size of the melt bath increases, the size of a single bead grows; hence, the thickness of a built wall increases as well [34,35]. In addition, following the findings in [34], at higher values, laser scanning velocity affects the melt pool

size less than laser power. At 200 W, it was not possible to grow a continuous wall, and at 230 W, the wall remained unstable along its entire length. The smallest thickness with stable formation was achieved in the power range of 260–350 W, with the wall thickness in the 320–350 W range showing the least deviation from the average value (Figure 7).

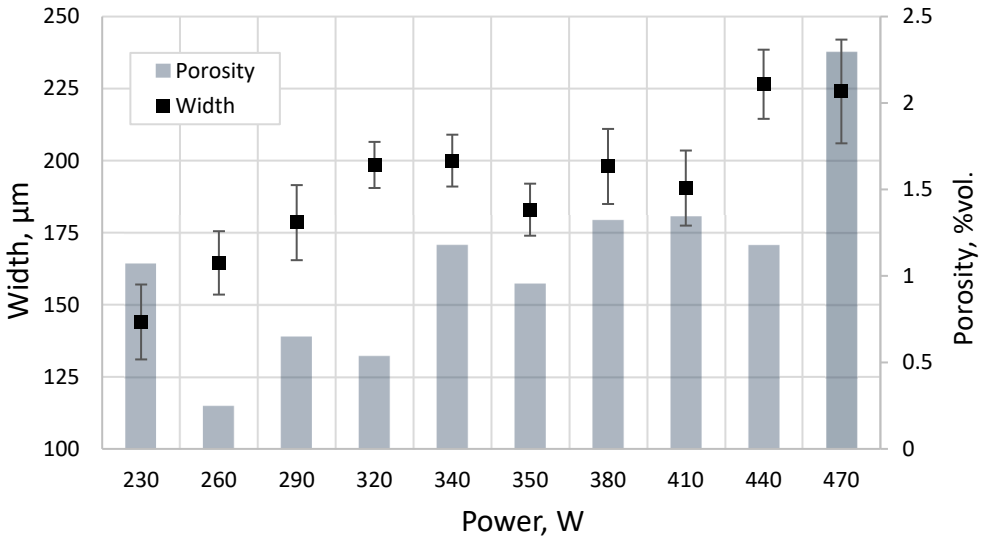

Figure 7. Change in wall thickness and porosity of single-scan walls depending on laser power.

The porosity factor was taken as an additional criterion for optimization to select the process parameters for thin-walled elements. The quantitative value of porosity in the samples was assessed using "Image J" software ver. 1.53t by determining the porosity fraction from the image of the cross-section (Table 4). The areas of various spherical pores were measured with an optical microscope and its software. With an increase in power, porosity is increased. The first noticeable manifestations of porosity can be seen in samples 4 and 5 (P = 290 and 320 W, respectively, Figure 8c,d). In sample 6 (340 W, Figure 8e), the pore size increases, and the number of pores rises. High porosity values remain until sample 11 (470 W, Figure 8j), where the average pore size decreases, but the quantity of pores significantly increases.

Thus, despite there being the lowest deviation of wall thickness from the average size at powers of 320–350 W, noticeable pores can be observed on the polished surface. Taking into account the combination of the geometric characteristics of the samples and the absence of visible melting defects as an optimization criterion, a rational mode can be considered with laser power P = 260 W and scanning speed V = 1500 mm/s.

The study of the microstructure of wall samples obtained through single-pass scanning revealed the presence of only one melt pool in a layer without any offset of its center, indicating the correct execution of the scanning strategy. The samples clearly show discrete layers, the boundaries of the melt pool (Figure 9a,b), and uniaxial dendrites elongated in the direction of heat dissipation (Figure 9a,b). The depth of the melt pool in the sample (see Figure 9) varies slightly, ranging from 11.97 µm to 36.68 µm. At high power (470 W), the development of dendrites, including second-order dendrites, in various orientations is observed, which is a consequence of overheating and a slowdown in the cooling rate (see Figure 10).

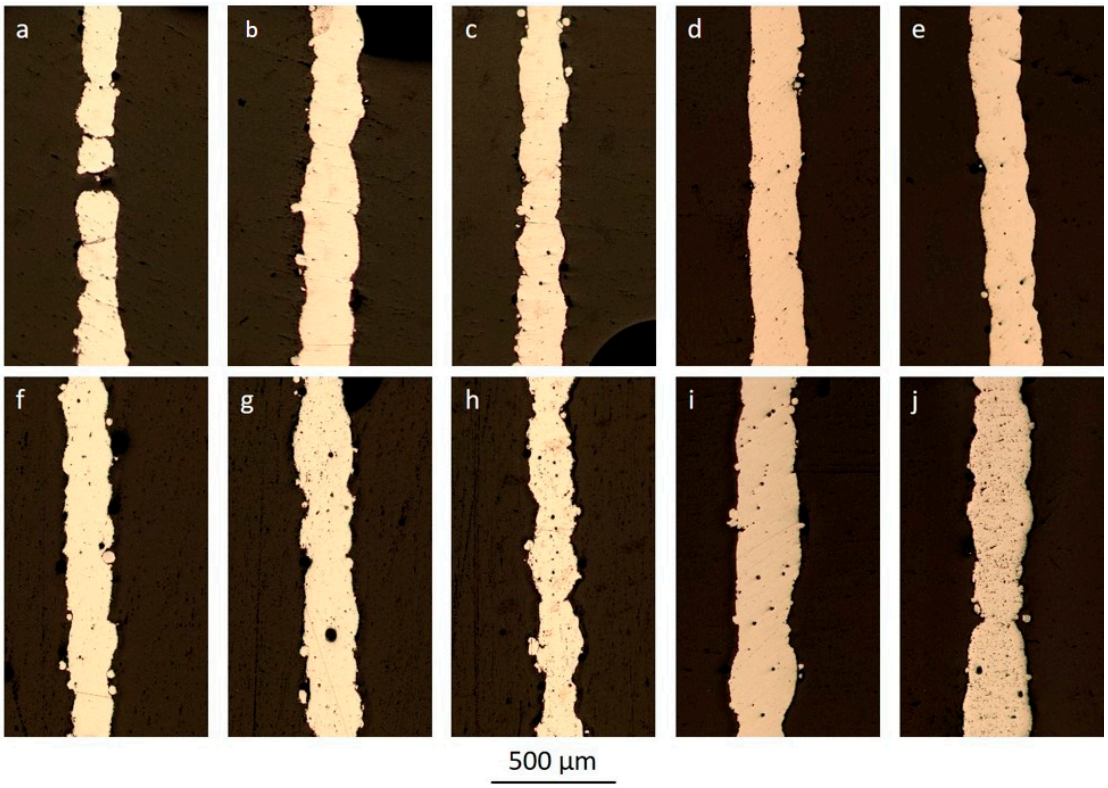

Figure 8. Cross-sections of single-pass walls obtained at scanning speed of 1500 mm/s and laser power of 230 W (**a**), 260 W (**b**), 290 W (**c**), 320 W (**d**), 340 W (**e**), 350 W (**f**), 380 W (**g**), 410 W (**h**), 440 W (**i**), and 470 W (**j**).

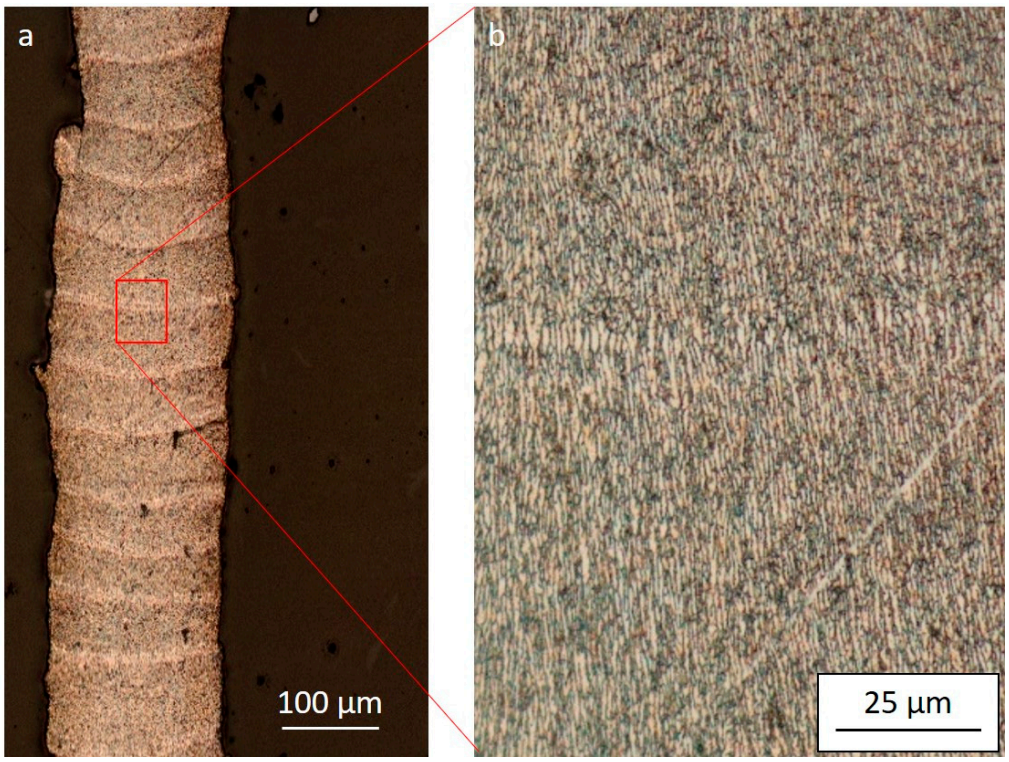

Figure 9. The microstructure of the wall obtained at a laser scanning speed of 1500 mm/s and a laser power of 260 W at a magnification of ×100 (**a**) and ×500 (**b**).

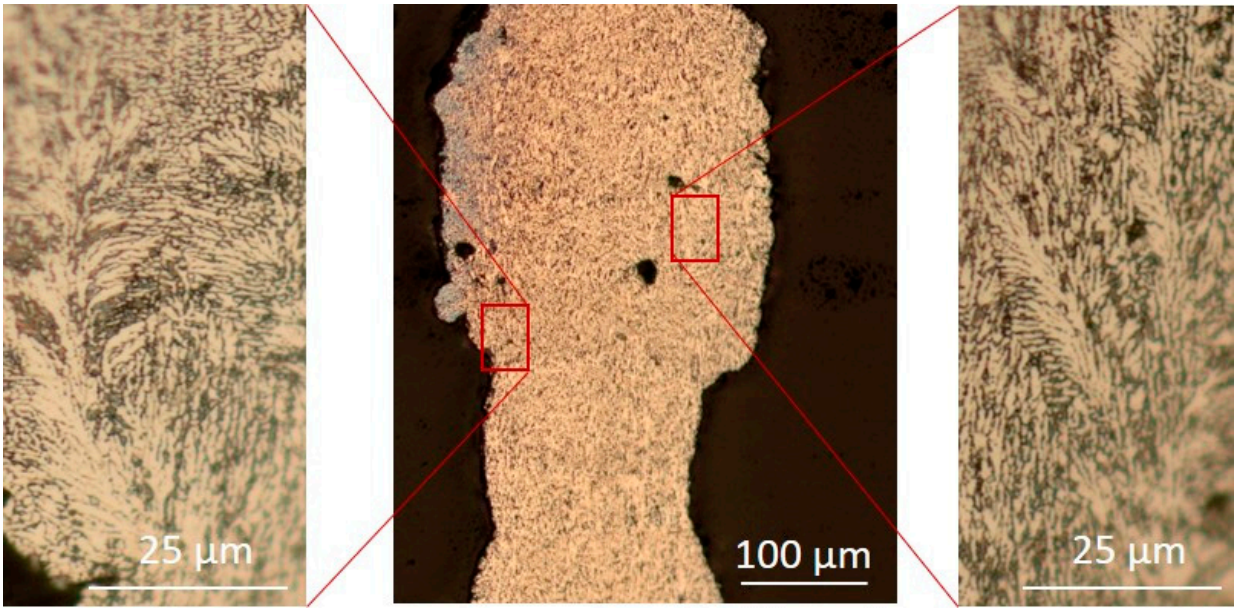

Figure 10. The microstructure of the wall obtained at a laser scanning speed of 1500 mm/s and a laser power of 470 W.

3.4. Study of Cellular Structures

Based on the parametric analysis of the process for producing thin walls from the alloy AlSi10Mg, the process parameters for the SLM of cellular structures were selected as follows: a scanning speed of 1500 mm/s, laser power of 260 W, layer thickness of 30 µm, laser spot diameter of 50 µm, and hatch distance of 0.15 mm. The sample, whose volume was replaced by cellular structures, was a cube measuring 20 × 20 × 20 mm, utilizing a Diamond lattice type (Figure 11). The elementary cell size was 5 × 5 × 5 mm, which, according to [36], is sufficient to characterize mechanical properties. No significant defects were detected in the microstructure of the sample. The grain size varies from submicron to 3–4 µm (Figure 12).

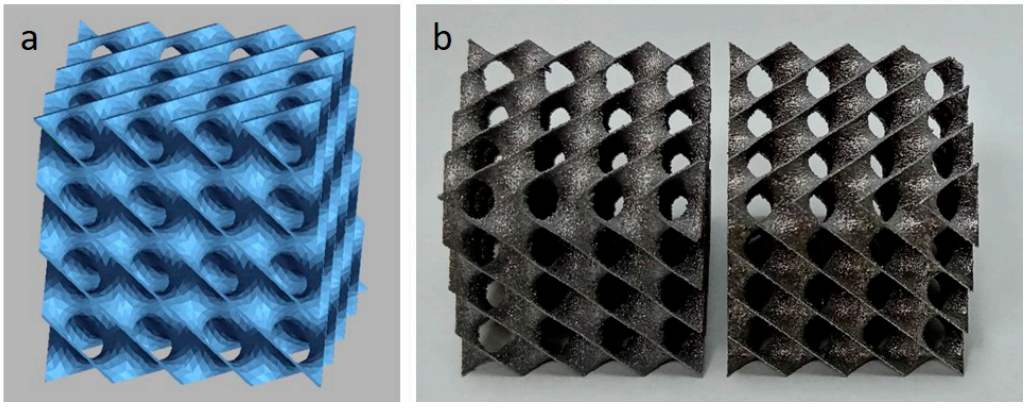

Figure 11. Model (**a**) and manufactured Diamond cellular structures with cell size of 5 × 5 × 5 mm (**b**).

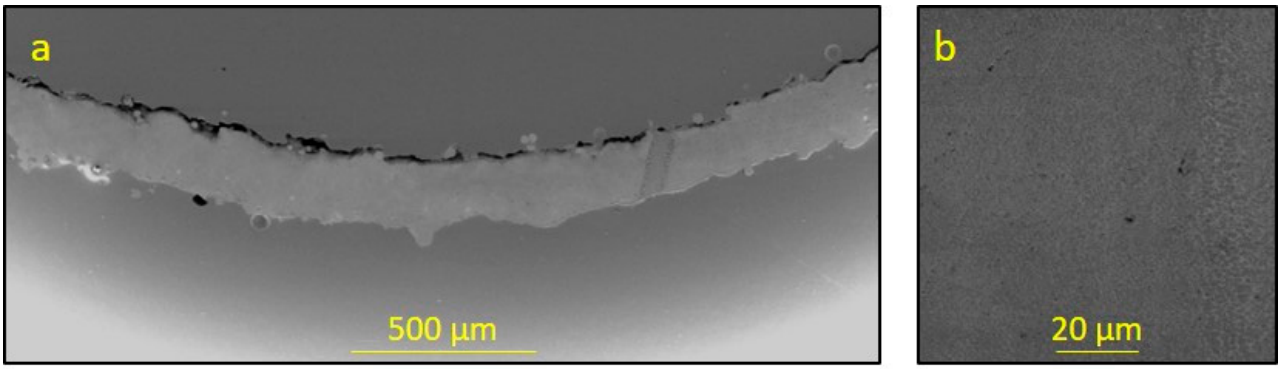

Figure 12. A cross-section of a thin-walled element of the Diamond lattice structure at ×140 (**a**) and ×5000 (**b**).

The study of the geometric accuracy of the manufactured structures was conducted using computer tomography at several sections located at 1.35 mm, 2.43 mm, and 8.84 mm from the surface and comparing them with the digital model (Figure 11). In these sections, the contour of the lattice structure is maximally straightened, forming straight lines for ease of measurement.

In each of the cross-sections, the thickness of the walls on the digital model and the printed samples was measured. As a result, the sample mean and confidence interval were found at a confidence level of 0.95. The deviation of the actual thickness from the nominal thickness was also determined as the difference between the wall thickness of the specimen and the wall thickness of the model. The results are presented in Table 5 and Figure 13. The contour of the model does not represent a straight line (due to the size of the unit polygon in the model), making measurements difficult. The nominal thickness of the model is 0.2 mm, and the deviation of the actual thickness in the first two sections is 0.015 mm and 0.011 mm, while in the third, it is close to zero.

Table 5. The results of measuring the Diamond cellular structure in sections.

Section	Distance from Top, mm	Wall Thickness (Tomography), mm	Wall Thickness (3D Model), mm	Deviation of Actual Thickness from Nominal, mm
1	1.35	0.215 ± 0.01	0.203 ± 0.006	0.12
2	2.43	0.211 ± 0.01	0.211 ± 0.008	0
3	8.84	0.200 ± 0.01	0.206 ± 0.004	0.006

The analysis of the obtained results shows that the process parameters used for growing bulk solid samples are not always optimal for printing thin elements due to differences in heat dissipation processes and the geometry of the melt pool. After parametrization, it was possible to establish process parameters for manufacturing thin-walled elements. Considering the results of microstructure studies (presence of defects: pores and cracks) and manufacturing accuracy, process parameters were selected that provide a wall thickness of 0.2 mm. In addition, the process parameters ensured a microstructure with uniaxial dendrites oriented in the direction of heat dissipation, which indicates a high cooling rate during crystallization, while tomographic studies showed the minimal deviation of the grown structure from the designed model.

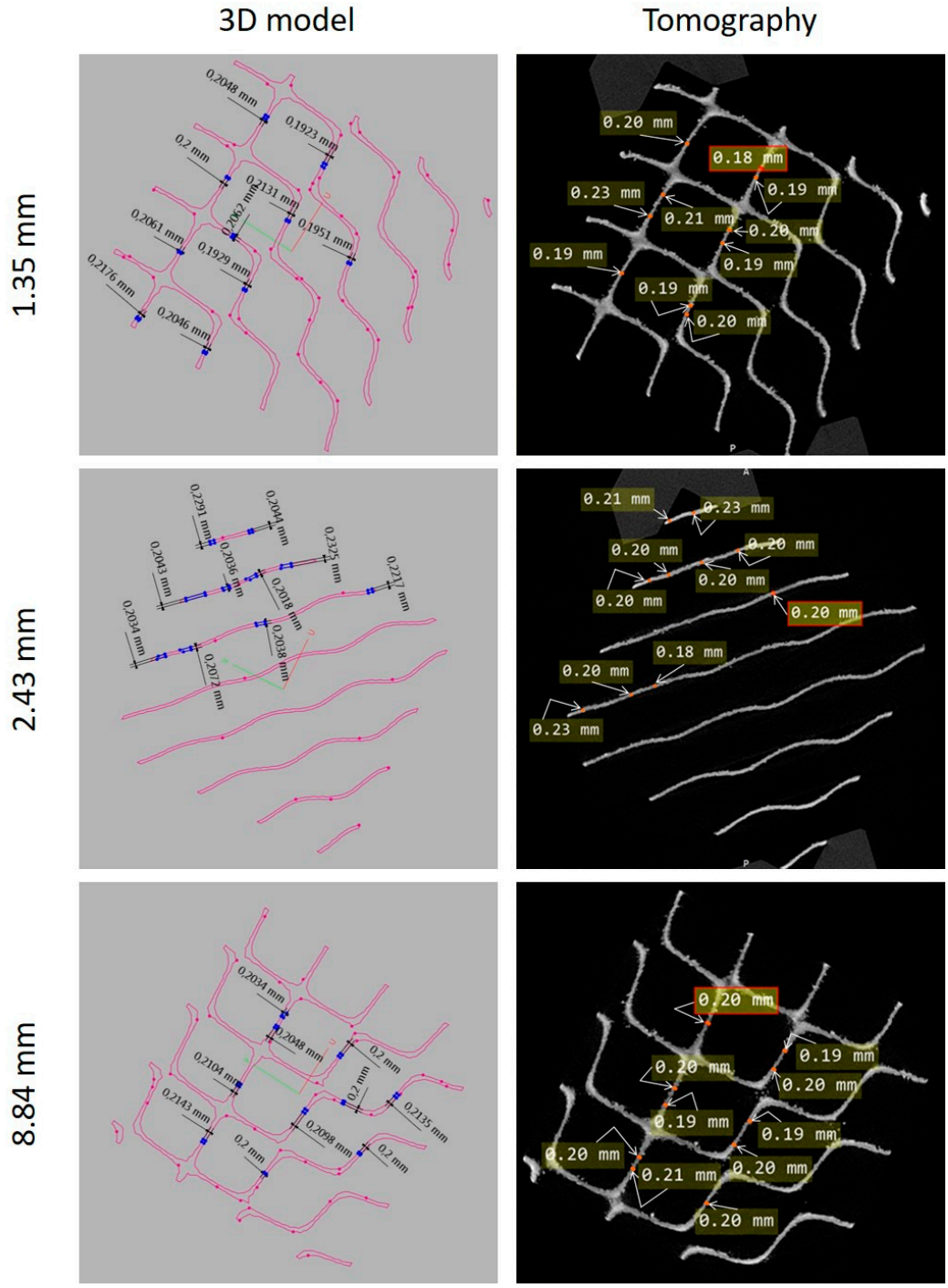

Figure 13. Results of Diamond cellular structure tomography.

3.5. Mechanical Behavior of Cellular Structures Based on Minimum Surface Area

The compression testing of the Diamond lattice structure made of the AlSi10Mg alloy was carried out on an Instron 5989 machine with video recording for each sample. In the initial phase, when the graph shows an increase in stress (Figure 14) to the peak values, elastic deformation occurs (Figure 14b). Each cell participates in load distribution, maintaining the overall stiffness and strength of the entire structure. Further compression that exceeds the critical load a cell can withstand leads to irreversible shape changes in cells, causing the structure to lose its ability to recover after the load. The load-bearing capacity of this row of cells sharply decreases, and the applied load leads to plastic deformation

and failure, reflected on the graph as a movement toward the minimum (Figure 15c). The graph's reversal indicates the start of the next row of cells working and also signals a return to elastic deformation. A new cell enters the process, restoring the functionality of the structure until the critical load is once again reached, initiating a new cycle of failure.

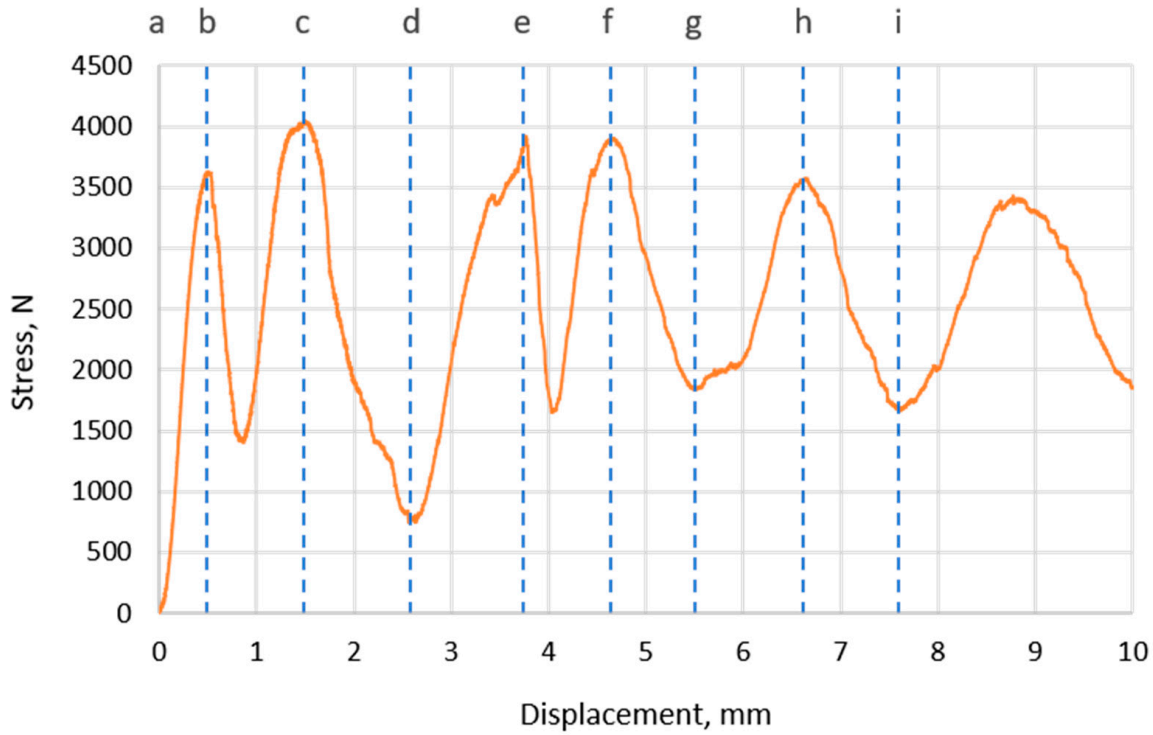

Figure 14. A compression stress–displacement curve of a Diamond cellular structure with a wall thickness of 0.2 mm. Letters refer to the state of a specimen in Figure 15.

It is noteworthy that in the shell-type Diamond cellular structure, each row of cells shows approximately the same load-bearing capacity, while the Diamond strut structure has the maximum resistance to compression only in the first row of cells, which significantly decreases after the formation of a shear band [37]. This band extends along the entire sample at a 45-degree angle to the load direction, reducing the overall load-bearing capacity of the structure. In the shell structure, failure occurs sequentially, starting from the top row of cells. Various types of failures of cellular structures under compression are known: the sequential collapse of cells in planes perpendicular to the direction of fabrication and loading, the brittle failure of cell walls, crack propagation through the lattice, and diagonal shear. In this case, the sequential collapse of cells in planes perpendicular to the direction of fabrication and loading is observed.

Thus, the graph becomes not only a reflection of the behavior of individual cells but also an illustration of the complex interaction between elastic and plastic deformations in the cellular structure.

The mechanical characteristics of Diamond-type cellular structures obtained from AlSi10Mg alloys using SLM are shown in Table 6.

Table 6. The results of mechanical tests.

Sample	Young's Modulus [GPa]	Yield Strength [MPa]	Stress Limit [MPa]
Diamond	26.351	8.063	8.947

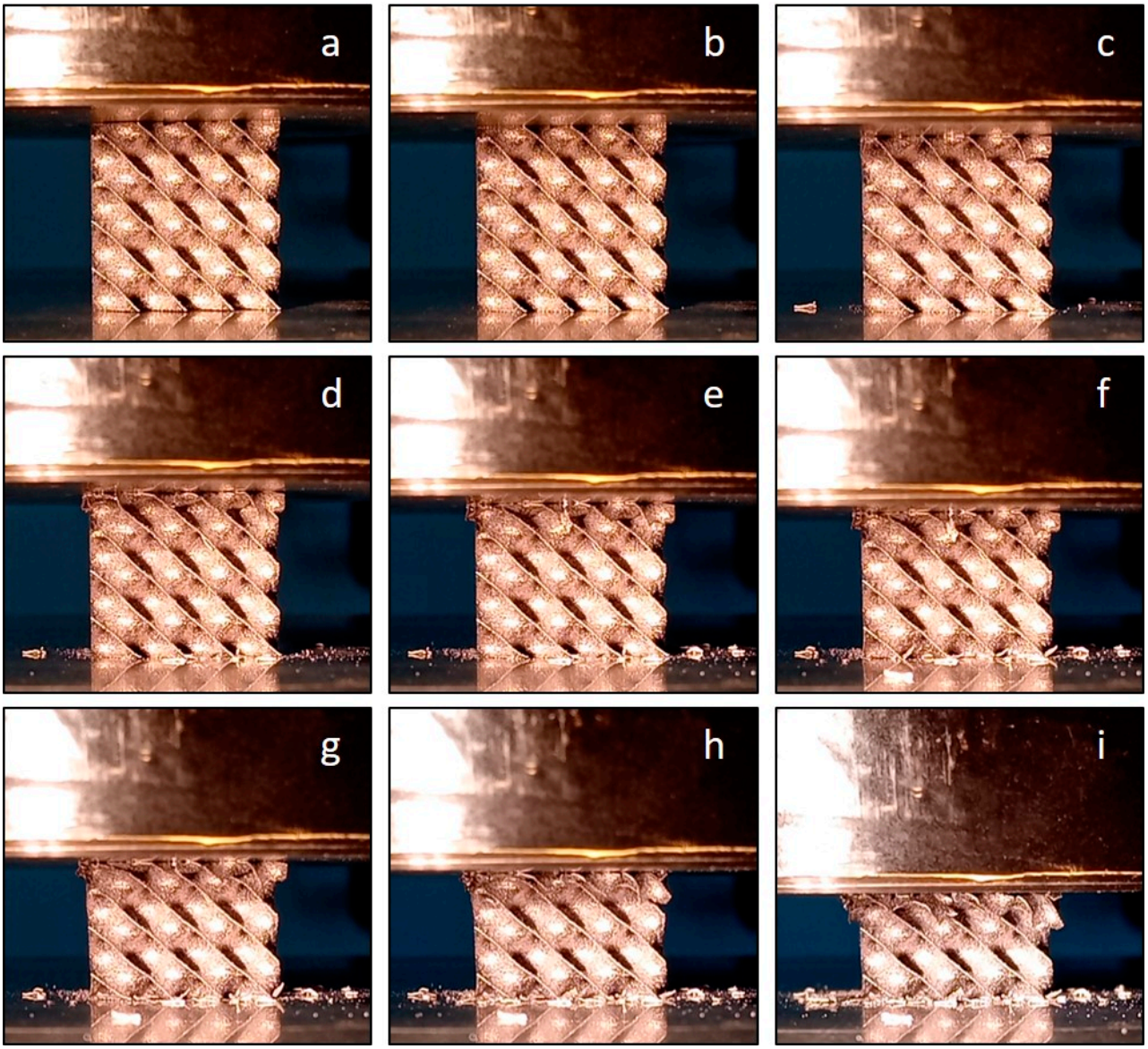

Figure 15. Images of the Diamond cellular structure with a wall thickness of 0.4 mm during mechanical testing: the state of the specimen at the beginning of the test (**a**) and the state of the specimen at a certain point on the stress–displacement curve Figure 14 (**b**–**i**).

The analysis of the mechanical characteristics of Diamond-type lattices indicates that this type of lattice, with a wall thickness of 0.2 mm, allows for the prevention of structural failure at low deformation due to localized damage and crack propagation. This is particularly important when considering the practical application of cellular structures for specific components.

For comparison, the compression testing of a Dimond cellular structure with an increased wall thickness of 0.6 mm was performed (Figure 16). The strain curve suggests another failure mode that corresponds to the diagonal shear and brittle fracture of cell walls. The formation of a diagonal shear band at an angle of 45° to the direction of loading is clearly observed (Figure 17). Thus, failure mode depends on wall thickness.

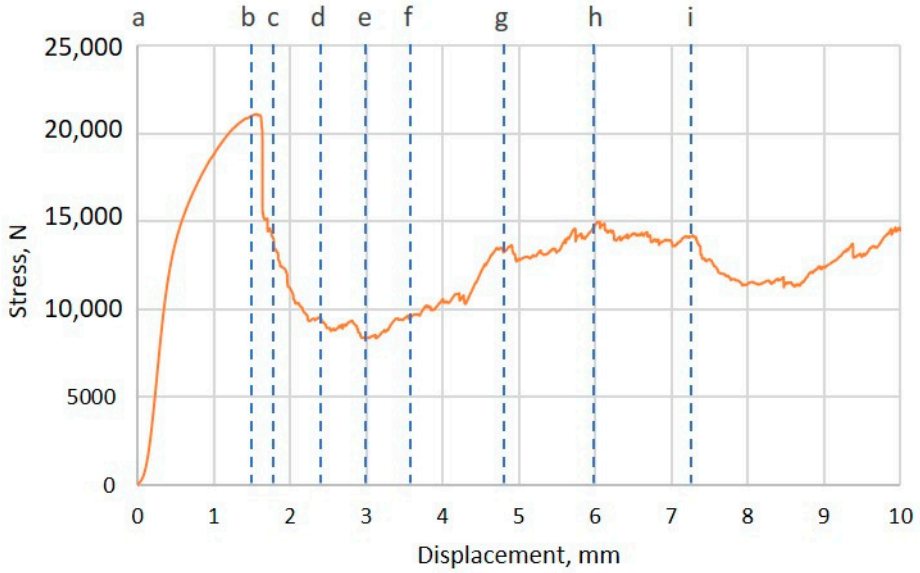

Figure 16. A compression stress–displacement curve of a Diamond cellular structure with a wall thickness of 0.6 mm. Letters refer to the state of a specimen in Figure 17.

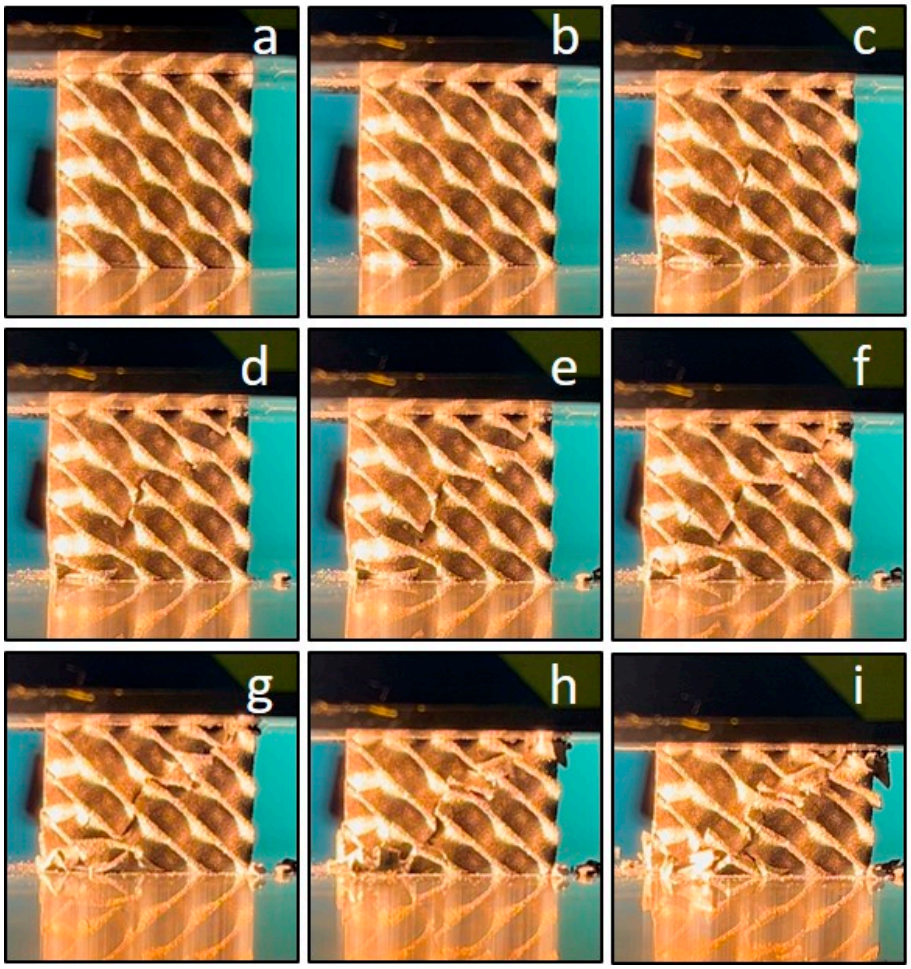

Figure 17. Images of the Diamond cellular structure with a wall thickness of 0.6 mm during mechanical testing: the state of the specimen at the beginning of the test (**a**) and the state of the specimen at a certain point on the stress–displacement curve Figure 16 (**b**–**i**).

4. Conclusions

The present study investigated thin-walled elements and shell-like Diamond lattice structures, made from the aluminum alloy AlSi10Mg using SLM technology. The conducted research demonstrated that the most optimal parameters for the SLM of the AlSi10Mg alloy, which ensure the minimal deviation from the specified size at a level of 5 μm and a minimal porosity of 0.1% vol., are a laser power of P = 260 W and a scanning speed of V = 1500 mm/s. It was observed that an increase in laser power results in a greater average wall thickness and porosity.

Furthermore, the application of a single-pass scanning strategy established a parameter window of 260–350 W, which provides the minimal thickness of the fused thin-walled elements while maintaining a porosity not exceeding 1% vol., the absence of cracks and lack of fusion, the reproducibility of the results, and the smallest deviation of thickness from the average value. A minimum thickness of 164.55 $\pm$ 10.12 μm, with a porosity of 0.1% vol., was also achieved at a laser power of P = 260 W and V = 1500 mm/s.

To validate the results under established modes, Diamond-type cellular structures with a cell size of 5 $\times$ 5 $\times$ 5 mm and a wall thickness of 0.2 mm and 0.6 mm were fabricated. The produced structures conformed in shape, size, and accuracy to the 3D model, and no microstructure defects were detected. Mechanical tests revealed that in this configuration of the cellular structure with a wall thickness of 0.2 mm, no brittle failure occurs across the entire construction under compression, resulting in the loss of load-bearing capacity. It was also observed that increasing wall thickness to 0.6 mm changes the failure mode and leads to brittle diagonal destruction.

Author Contributions: Conceptualization, T.T.; methodology, T.T. and P.P.; software, N.B.; validation, R.K., T.T. and P.P.; formal analysis, A.G. and R.K.; investigation, D.S., N.B. and T.T.; resources, T.T. and S.N.G.; data curation, A.G. and T.T.; writing—original draft preparation, P.P.; writing—review and editing, T.T., P.P. and A.G.; visualization, N.B., D.S. and P.P.; supervision, S.N.G.; project administration, T.T.; funding acquisition, S.N.G. All authors have read and agreed to the published version of the manuscript.

Funding: This work was supported by the Russian Science Foundation (Grant Agreement No. 23-19-00334, 15 May 2023).

Institutional Review Board Statement: Not applicable.

Informed Consent Statement: Not applicable.

Data Availability Statement: The original contributions presented in the study are included in this article; further inquiries can be directed to the corresponding author.

Acknowledgments: The experiments were conducted using the equipment of the State Engineering Center of Moscow State University of Technology "STANKIN".

Conflicts of Interest: The authors declare no conflicts of interest.

References

1. *ISO/ASTM 52900:2021*; Additive Manufacturing—General Principles—Fundamentals and Vocabulary. International Organization for Standarization: London, UK, 2021. Available online: https://www.iso.org/standard/74514.html?browse=tc (accessed on 16 February 2023).
2. Chen, L.Y.; Liang, S.X.; Liu, Y.; Zhang, L.C. Additive manufacturing of metallic lattice structures: Unconstrained design, accurate fabrication, fascinated performances, and challenges. *Mater. Sci. Eng. R Rep.* **2021**, *146*, 100648. [CrossRef]
3. Zhang, Y.; Aiyiti, W.; Du, S.; Jia, R.; Jiang, H. Design and mechanical behaviours of a novel tantalum lattice structure fabricated by SLM. *Virtual Phys. Prototyp.* **2023**, *18*, e2192702. [CrossRef]
4. Rahmani, R.; Karimi, J.; Resende, P.R.; Abrantes, J.C.C.; Lopes, S.I. Overview of Selective Laser Melting for Industry 5.0: Toward Customizable, Sustainable, and Human-Centric Technologies. *Machines* **2023**, *11*, 522. [CrossRef]
5. Grigoriev, S.N.; Tarasova, T.V. Possibilities of the technology of additive production for making complex-shape parts and depositing functional coatings from metallic powders. *Met. Sci. Heat Treat.* **2016**, *57*, 579–584. [CrossRef]
6. Gao, B.; Zhao, H.; Peng, L.; Sun, Z. A Review of Research Progress in Selective Laser Melting (SLM). *Micromachines* **2023**, *14*, 57. [CrossRef] [PubMed]

7. Gokuldoss, P.K.; Kolla, S.; Eckert, J. Additive Manufacturing Processes: Selective Laser Melting, Electron Beam Melting and Binder Jetting—Selection Guidelines. *Materials* **2017**, *10*, 672. [CrossRef]
8. Al-Ketan, O.; Rowshan, R.; Al-Rub, R.A. Topology-mechanical property relationship of 3D printed strut, skeletal, and sheet based periodic metallic cellular materials. *Addit. Manuf.* **2018**, *19*, 167–183. [CrossRef]
9. Li, Z.H.; Nie, Y.F.; Liu, B.; Kuai, Z.Z.; Zhao, M.; Liu, F. Mechanical properties of AlSi10Mg lattice structures fabricated by selective laser melting. *Mater. Des.* **2020**, *192*, 108709. [CrossRef]
10. Alomar, Z.; Concli, F. A review of the selective laser melting lattice structures and their numerical models. *Adv. Eng. Mater.* **2020**, *22*, 2000611. [CrossRef]
11. Pan, C.; Han, Y.; Lu, J. Design and Optimization of Lattice Structures: A Review. *Appl. Sci.* **2020**, *10*, 6374. [CrossRef]
12. Zhang, L.; Song, B.; Fu, J.J.; Wei, S.S.; Yang, L.; Yan, C.Z.; Li, H.; Gao, L.; Shi, Y.S. Topology-optimized lattice structures with simultaneously high stiffness and light weight fabricated by selective laser melting: Design, manufacturing and characterization. *J. Manuf. Process.* **2020**, *56*, 1166–1177. [CrossRef]
13. Zhang, C.; Zheng, H.; Yang, L.; Li, Y.; Jin, J.; Cao, W.; Yan, C.; Shi, Y. Mechanical responses of sheet-based gyroid-type triply periodic minimal surface lattice structures fabricated using selective laser melting. *Mater. Des.* **2022**, *214*, 110407. [CrossRef]
14. Evans, S.; Jones, E.; Fox, P.; Sutcliffe, C. Photogrammetric analysis of additive manufactured metallic open cell porous structures. *Rapid Prototyp. J.* **2018**, *24*, 1380–1391. [CrossRef]
15. Favre, J.; Lohmuller, P.; Piotrowski, B.; Kenzari, S.; Laheurte, P.; Meraghni, F. A continuous crystallographic approach to generate cubic lattices and its effect on relative stiffness of architectured materials. *Add. Manuf.* **2018**, *21*, 359–368. [CrossRef]
16. Bai, L.; Zhang, J.; Xiong, Y.; Chen, X.; Sun, Y.; Gong, C.; Pu, H.; Wu, X.; Luo, J. Influence of unit cell pose on the mechanical properties of Ti6Al4V lattice structures manufactured by selective laser melting. *Add. Manuf.* **2020**, *34*, 101222. [CrossRef]
17. Refai, K.; Brugger, C.; Montemurro, M.; Saintier, N. An experimental and numerical study of the high cycle multiaxial fatigue strength of titanium lattice structures produced by Selective Laser Melting (SLM). *Int. J. Fatigue* **2020**, *138*, 105623. [CrossRef]
18. Hou, Y.; Li, Y.; Cai, X.; Pan, C.; Wang, J.; Zhang, W.; Xu, P.; Fan, Z.; Gao, Y.; Li, Z.; et al. Mechanical response and response mechanism of AlSi10Mg porous structures manufactured by laser powder bed fusion: Experimental, theoretical and numerical studies. *Mater. Sci. Eng. A* **2022**, *849*, 143381. [CrossRef]
19. Maskery, I.; Aboulkhair, N.T.; Aremu, A.O.; Tuck, C.J.; Ashcroft, I.A. Compressive failure modes and energy absorption in additively manufactured double gyroid lattices. *Addit. Manuf.* **2017**, *16*, 24–29.
20. Zhang, L.; Feih, S.; Daynes, S.; Chang, S.; Wang, M.Y.; Wei, J.; Lu, W.F. Energy absorption characteristics of metallic triply periodic minimal surface sheet structures under compressive loading. *Addit. Manuf.* **2018**, *23*, 505–515. [CrossRef]
21. Moustafa, A.R.; Dinwiddie, R.B.; Pawlowski, A.E.; Splitter, D.A.; Shyam, A.; Cordero, Z.C. Mesostructure and porosity effects on the thermal conductivity of additively manufactured interpenetrating phase composites. *Addit. Manuf.* **2018**, *22*, 223–229. [CrossRef]
22. Khanna, P.; Sood, S.; Mishra, P.; Bharadwaj, V.; Aggarwal, A.; Singh, S.J. Analysis of compression and energy absorption behaviour of SLM printed AlSi10Mg triply periodic minimal surface lattice structures. *Structures* **2024**, *64*, 106580. [CrossRef]
23. Yan, C.; Hao, L.; Hussein, A.; Bubb, S.L.; Young, P.; Raymont, D. Evaluation of light-weight AlSi10Mg periodic cellular lattice structures fabricated via direct metal laser sintering. *J. Mater. Process. Technol.* **2014**, *214*, 856–864. [CrossRef]
24. Soul, H.; Terriault, P.; Brailovski, V. The Static and Fatigue Behavior of AlSiMg Alloy Plain, Notched, and Diamond Lattice Specimens Fabricated by Laser Powder Bed Fusion. *J. Manuf. Mater. Process.* **2018**, *2*, 25. [CrossRef]
25. Yu, T.; Hyer, H.; Sohn, Y.; Bai, Y.; Wu, D. Structure-property relationship in high strength and lightweight AlSi10Mg microlattices fabricated by selective laser melting. *Mater. Des.* **2019**, *182*, 108062. [CrossRef]
26. Nie, Y.; Tang, Q.; Zhao, M.; Song, J. Effect of heat treatment on mechanical properties, failure modes and energy absorption characteristics of lattice skeleton and sheet structures fabricated by SLM. *JMR&T* **2023**, *26*, 4925–4941. [CrossRef]
27. Song, J.; Wang, M.; Li, D.; Zhang, J. Deformation and Energy Absorption Performance of Functionally Graded TPMS Structures Fabricated by Selective Laser Melting. *Appl. Sci.* **2024**, *14*, 2064. [CrossRef]
28. Baroutaji, A.; Arjunan, A.; Beal, J.; Robinson, J.; Coroado, J. The Influence of Atmospheric Oxygen Content on the Mechanical Properties of Selectively Laser Melted AlSi10Mg TPMS-Based Lattice. *Materials* **2023**, *16*, 430. [CrossRef]
29. Cosma, C.; Drstvensek, I.; Berce, P.; Prunean, S.; Legutko, S.; Popa, C.; Balc, N. Physical–mechanical characteristics and microstructure of Ti6Al7Nb lattice structures manufactured by selective laser melting. *Materials* **2020**, *13*, 4123. [CrossRef]
30. Ge, J.; Yan, X.; Lei, Y.; Ahmed, M.; O'Reilly, P.; Zhang, C.; Lupoi, R.; Yin, S. A detailed analysis on the microstructure and compressive properties of selective laser melted Ti6Al4V lattice structures. *Mater. Des.* **2021**, *198*, 109292.
31. Choy, S.Y.; Sun, C.N.; Leong, K.F.; Wei, J. Compressive properties of functionally graded lattice structures manufactured by selective laser melting. *Mater. Des.* **2017**, *131*, 112–120. [CrossRef]
32. *ASTM E8–08–16a*; Test Methods for Tension Testing of Metallic Materials; Annual Book of ASTM Standards. ASTM International: West Conshohocken, PA, USA, 2008.
33. Tarasova, T.; Podrabinnik, P.; Babushkin, N.; Khmyrov, R.; Grigoriev, S. The quality of thin-walled structures of alsi10mg produced by selective laser melting. *High Temp. Mater. Process.* **2024**, *28*, 29–39. [CrossRef]
34. Yadroitsev, I.; Yadroitsava, I.; Du Plessis, A.; MacDonald, E. *Fundamentals of Laser Powder Bed Fusion of Metals*; Elsevier: Amsterdam, The Netherlands, 2021; pp. 79–117.

35. Dilip, J.J.S.; Zhang, S.; Teng, C.; Zeng, K.; Robinson, C.; Pal, D.; Stucker, B. Influence of processing parameters on the evolution of melt pool, porosity, and microstructures in Ti-6Al-4V alloy parts fabricated by selective laser melting. *Prog. Addit. Manuf.* **2017**, *2*, 157–167. [CrossRef]
36. Bobbert, F.S.L.; Lietaert, K.; Eftekhari, A.A.; Pouran, B.; Ahmadi, S.M.; Weinans, H.; Zadpoor, A.A. Additively manufactured metallic porous biomaterials based on minimal surfaces: A unique combination of topological, mechanical, and mass transport properties. *Acta Biomater.* **2017**, *53*, 572–584. [CrossRef] [PubMed]
37. Qiu, C.; Yue, S.; Adkins, N.J.; Ward, M.; Hassanin, H.; Lee, P.D.; Withers, P.J.; Attallah, M.M. Influence of processing conditions on strut structure and compressive properties of cellular lattice structures fabricated by selective laser melting. *Mater. Sci. Eng. A* **2015**, *628*, 188–197. [CrossRef]